Nanoscale

PAPER

View Article Online
View Journal | View Issue

Cite this: *Nanoscale*, 2023, **15**, 14858

Gold nanohexagrams *via* active surface growth under sole CTAB control†

An Su,[a,b] Qian Wang,[a,b] Liping Huang,[a,b] Yonglong Zheng,[a,b,c] Yawen Wang[c] and Hongyu Chen*[a,b]

Received 23rd June 2023,
Accepted 23rd August 2023

DOI: 10.1039/d3nr03006g

rsc.li/nanoscale

The synthesis of homochiral nanostructures involves not only the chiral ligand, but also CTAB. The latter is often treated as a weak ligand unable to compete with the thiol-based chiral ligand. Here, we show that CTAB alone is able to induce Active Surface Growth on Au nanoplates, giving curved tips and steep ridges in the resulting nano-hexagrams. The growth materials (Au^0) are diverted to a few active sites, whereas the rest of the Au surfaces are inhibited. Modulation of the growth rate by the ratio of ascorbic acid to Au precursor gives a continuous change of the growth modes, explaining the main trends of shape evolution and the inequivalent growth of the equivalent surfaces. With only CTAB as the ligand, the fact that ridges and spikes could be formed in defiance of facet control suggests that the role of CTAB cannot be ignored in the chiral synthesis and that the precise modulation of the Active Surface Growth could be the key to rational synthetic controls.

Introduction

The adjective 'chiral' is used to describe objects that have neither mirror nor inversion symmetry.[1] Chiral molecules are of great importance because of their biological functions, which are the result of their specific interactions with chiral biomolecules. In relation to nanomaterials, asymmetric catalysis and chiral separation both involve interactions with chiral molecules, so there is a great deal of interest in chiral structures. Recent advances in synthetic capabilities have extended this interest to larger-scale symmetry breaking, for instance in molecular rotors and magnetic nano-propellers,[2–4] where chirality is a prerequisite for converting rotational motion into translational propulsion.

Chiral induction from small organic molecules (typically <1 nm) to nanostructures (~100 nm) spans two orders of magnitude. As such, the organization of chiral molecules is essential for understanding and controlling chiral induction. Unfortunately, it has proven extremely difficult to obtain information on the nature of ligand packing on the surface of nanostructures. While static ligand packing (self-assembled monolayers, *etc.*) on well-defined facets has been studied *via* scanning tunnelling microscopy,[5] it remains a great challenge to probe dynamic ligand packing during the growth of nanostructures and, more specifically, on the interplay between materials deposition and ligand organization.

There are only a few principles known for controlling nanosynthesis, either involving facet control for nanocrystals or minimal surface for nanospheres. Importantly, there has as yet been no example of a chiral nanostructure in either of these two categories. The surfaces of typical chiral nanostructures are not flat or smooth, but have complex patterns of ridges and valleys. We therefore cannot rely on stable facets and minimal surface energy to explain the chiral surface features. They require a different set of explanations.

The most successful current system of chiral induction involves thiol-containing cysteine or its derivatives, which bind strongly on Au nanostructures.[6–11] Importantly, these previous studies have all used hexadecyltrimethylammonium bromide (CTAB) as the surfactant during synthesis, but its role is rarely discussed and only a few works recorded the effects of CTAB in the absence of chiral ligands.[8,9,12]

CTAB is a highly abnormal ligand/surfactant: it contains a tertiary amine and there is therefore no lone pair available for the formation of coordination bonds to metal atoms. The surfaces of noble metal nanoparticles are generally neutral, with perhaps a few positive charges. For this reason, it is difficult to attract a positively charged tertiary amine group unless anions are involved. Despite extensive usage of CTAB, there is no clear assignment for the CTA^+ and Br^- ions in CTAB binding, other

---

[a] *Department of Chemistry, School of Science and Research Center for Industries of the Future, Westlake University, 600 Dunyu Road, Hangzhou 310030, Zhejiang Province, China. E-mail: chenhongyu@westlake.edu.cn*

[b] *Institute of Natural Sciences, Westlake Institute for Advanced Study, 18 Shilongshan Road, Hangzhou 310024, Zhejiang Province, China*

[c] *Institute of Advanced Synthesis (IAS), and School of Chemistry and Molecular Engineering, Jiangsu National Synergetic Innovation Centre for Advanced Materials, Nanjing Tech University, Nanjing, 211816, China*

† Electronic supplementary information (ESI) available. See DOI: **https://doi.org/10.1039/d3nr03006g**

than that the binding is cooperative[13,14] and that CTAB forms a bilayer structure.[15,16]

We have previously shown that CTAB is not as weak a ligand as is commonly perceived. So long as the rate of Au deposition exceeds the limit imposed by ligand dynamics (the choked condition),[17] a divergent growth mode ensues, with deposition focused on the active sites and the rest of the nanoparticle surface inhibited. This 'Active Surface Growth' (ASG) mode is typically observed with strong ligands[18] where it leads to inequivalent growth of equivalent facets. To take a broader view, this growth mode could provide an alternative explanation for the bulged growth features on nanoparticles, such as spikes, ridges, and chiral patterns.

In light of the CTAB-induced ASG and other site-selective growths,[19] the combined use of CTAB and thiol-based strong ligands in chiral induction is more complex than expected, as we should not dismiss the role of CTAB simply because a stronger ligand is present. More specifically, if CTAB alone can induce the formation of ridges, and thiol-based ligand alone gives random spiky nanoparticles, we have to assume that the two ligands play cooperative roles. Thus, understanding the role of CTAB emerges as an important reference or baseline for chiral induction.

Here, we show that CTAB alone can induce the formation of ridges on flat nanoplates, giving nanohexagrams with raised ridges at the middle of each arm. The raised ridges are highly correlated to active growth sites in the horizontal direction, suggesting that they may be vertical traces left by the advancing active growth sites. The growth behavior is generally characteristic of Active Surface Growth, with curved horizontal tips, strong correlations between each ridge and tip, and steep ridges and craters.

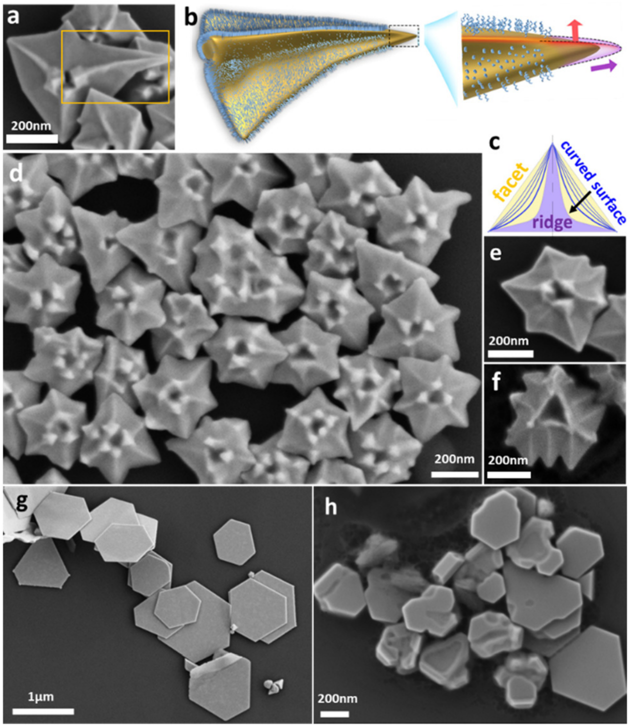

Fig. 1 Au nanohexagram *via* Active Surface Growth. (a) SEM image and (b) schematics explaining the strong correlation between the tip and ridge, by assigning the ridge as the vertical component of the active site (tip). (c) Schematics illustrating the difference between facet, curved surface, and ridge. (d) The Au nanohexagrams prepared by the standard condition. (e and f) Abnormal examples where the tips and ridges are not pointing at the usual directions, highlighting their strong correlation. (g and h) Product nanostructures after addition of I^- with 0.1 mM (0.42% I^-/Br^-) and 5 μM (0.021% I^-/Br^-) concentration, respectively.

Results and discussion

The nanohexagrams were synthesized in a seed-mediated growth from triangular Au nanoplates: a standard growth solution comprising the surfactant CTAB (15.2 mM), the Au source $HAuCl_4$ (0.095 mM), and the reductant ascorbic acid (AA, 9.1 mM) was prepared (with AA/$HAuCl_4$ = 96). Within a few seconds, 50 μL of the as-synthesized Au nanoplates (Fig. 3b, average length = 150 nm, thickness = 8 nm) were added under vigorous vortexing, and the mixture was maintained at 30 °C for 3 h. The product nanostructures were isolated by centrifugation, purified, and then characterized.

Fig. 1d shows the scanning electron microscopy (SEM) images of the nanohexagrams, where the most prominent feature is that their surface is not flat, unlike typical nanocrystals with flat facets and regular angles. There are 6 corners for each nanohexagram, with 3 arising from the corners of the initial triangular nanoplate, and 3 emerging corners (more for the abnormal cases) at middle of each edge. There is concave pit at the center of each nanohexagram with vertical spikes at its edge, and there is a raised ridge connecting each corner to the center. When viewed from a dihedral angle, the ridges appear as a curved surface without a fixed angle, as shown in the schematic illustration (Fig. 1c), which should not be perceived as the modified edges between adjacent facets. These ridges are remarkably similar to the ridges in the chiral patterns reported in the literature,[7,20] though they are not expected to give any chiral signal for the lack of chiral inducer. With only CTAB as the surfactant, it provides a more basic system for understanding the origin of the raised ridges, than the systems with combined use of CTAB and chiral ligand.

Fig. 1a, e and f show the occasional nanohexagrams (<5%) found with abnormal tips and ridges. More specifically, one of the tips in Fig. 1a has extended to extra length, where its orientation has obviously deviated from the "correct" direction and the ridge curves correspondingly. In Fig. 1e, there are two ridges that are not parallel to each other, with one obviously curved ridge. In Fig. 1f, the extra ridges are not pointed at the center, but to the internal corners of the triangular pit. These extraordinary examples show that the ridges are highly correlated to the tips. Indeed, no exception was found in our survey of over 800 nanoparticles across different reaction conditions. The fact that the ridges could curve and point to random directions is a strong indication that they do not arise from the facets or lattice with fixed orientations, likely with a strong influence from the dynamic growth conditions.

In our attempt to modulate the CTAB binding strength, we doped CTAB with a tiny fraction of I^- and replaced CTAB with the Cl^- counterpart CTAC. The former reaction (0.1 mM, 0.42% I^-/Br^-) gave thinner and larger nanoplates (Fig. 1g) that have much "cleaner" surface. Reducing the I^- concentration (5 μM, 0.021% I^-/Br^-, Fig. 1h) led to nanoplates with a few valleys, showing strong inhibition of the vertical growth and clear involvement of the anions. It also provides a control experiment to show that our CTAB reagent does not contain a significant amount of the impurity I^-.[21] On the other hand, the latter reaction led to significant vertical growth (Fig. S1a†), similar as the stellated octahedrons previously reported.[13] Besides, replacing CTAB with NaBr gave irregular nanoplates with random bulges (Fig. S1b†), suggesting that the anions alone are insufficient and that the growth control is likely also regulated by the orderly packing of the CTA^+ cations. That is, the CTA^+ and Br^- are strongly cooperative.[14]

In the literature, it is known that the binding energy of halides scales with their polarizability ($I^- > Br^- > Cl^-$) and the crystal facet (Au(111) > Au(110) > Au(100)).[22] The trends are generally consistent with the observed facet selectivity and with the competition between the broadly defined vertical and horizontal growth. More specifically, the nanoplate (111) surface is preferentially inhibited by I^- and the extent of vertical growth increases from I^- (flat nanoplates) to Br^- (spikes and ridges) and Cl^- (stellated extrusions). However, these arguments are still insufficient to explain the specific surface patterns, which is the focus of the following study.

The unfixed tips and ridges are characteristic of ASG:[18] the flat (111) facets of the initial nanoplate seeds have partially remain flat and partially raised into ridges, indicating inequivalent growth of the initially equivalent sites. Such a divergent growth mode cannot be explained by the stable facets or minimal surface energy. According to our previous hypothesis, the rate of Au deposition has probably exceeded the limit (the choked condition) allowed by the association-dissociation dynamics of CTAB.[17] As illustrated in Fig. 1b, the excess Au is diverted to a few active sites (tips and ridges), where the freshly grown surface has even fewer ligands, further promoting the growth. In other words, the choked condition is essential for initiating and maintaining the active sites, where the constant deposition establishes a ligand-deficient state against the ever-incoming ligands. It is a kinetic control in defiance of the stable facets and the minimal surface area (the thermodynamic factors).

On the basis of these arguments and the strong correlation between the tips and ridges, we speculate that the ridge merely reflects the vertical component of the growth at the active tip. Basically, the more rapid growth at the horizontal tip is "spilled over" to the vertical direction, where the faster deposition leads to fewer ligands. In the dynamic competition of the ASG, this initial difference is sufficient to cause multiple turnovers of "more deposition" and "fewer ligands", eventually leading to the ridge formation.

The nanohexagrams are in general too thick for high-resolution transmission electron microscopy (HRTEM). When the electron beam is incident on the [211] zone axis of the nanohexagram, the selected area electron diffraction (SAED) patterns are obtained. As shown in Fig. 2b, the entire nanoparticle gives a clean diffraction pattern indicating a high crystallinity. Careful analysis shows that in addition to the diffraction spots of {111}, {113} and {022}, weak spots with *d*-spacing of 2.47 Å is also observed between {113} and the transmitted spot, which does not belong to a single crystal. It can be explained as forbidden 1/2 {113} diffraction or hcp {1010} diffraction, arising from either a twin boundary or stacking fault,[7] which is likely inherited from the nanoplate seed. As shown in Fig. S2c–h,† the 6 corners of the nanohexagram show similar diffraction patterns, confirming that the lattice structure is highly consistent including the twin boundary. For the nanohexagram with abnormal tips and ridges (Fig. 2c), the diffraction patterns (Fig. 2d) confirm a highly crystalline structure with no apparent defects, and the Fourier transformation patterns of the selected areas in Fig. S3f–k† further verify the consistent lattice structure across the particle. On these bases, the nanohexagram has a pseudo-single-crystallinity, which is surprising given its complex morphology. Basically, the ASG is an external control, where the non-uniform ligand conditions determine the sites of growth, but all sites grow epitaxially, with no need to involve new defects.[9]

The temporal evolution of the nanohexagrams is shown in Fig. 3. Fig. 3a illustrates the horizontal and vertical evolution of the morphology; the colors green, orange, and yellow corres-

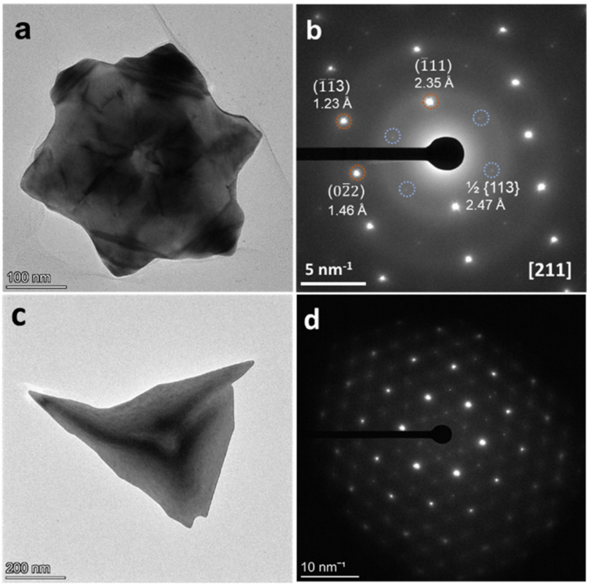

Fig. 2 The pseudo-single-crystallinity of the nanohexagram. (a) TEM image of a typical nanohexagram. (b) SAED pattern of the entire nanohexagram aligned to the [211] zone axis, the *d*-spacing with 2.35 Å, 1.23 Å, 1.46 Å, 2.47 Å correspond to {111}, {113}, {022} and 1/2{113} respectively. (c) TEM image of a nanohexagram with abnormal tips and ridges. (d) SAED pattern of the entire nanohexagram.

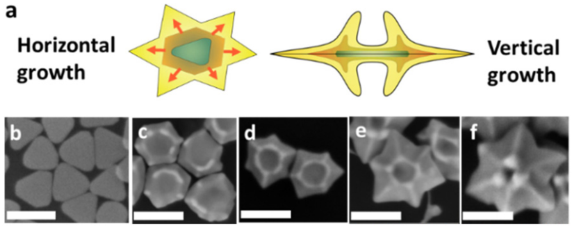

Fig. 3 Understanding the growth mode. (a) Schematics illustrating the separated components of the horizontal and vertical growth, where the green, orange, and yellow color represent 3 stages of morphology; (b) the initial triangular nanoplate seed; (c–f) temporal evolution of the Au nanohexagram at 20, 40, 90, and 180 min, respectively. All scale bars are 200 nm.

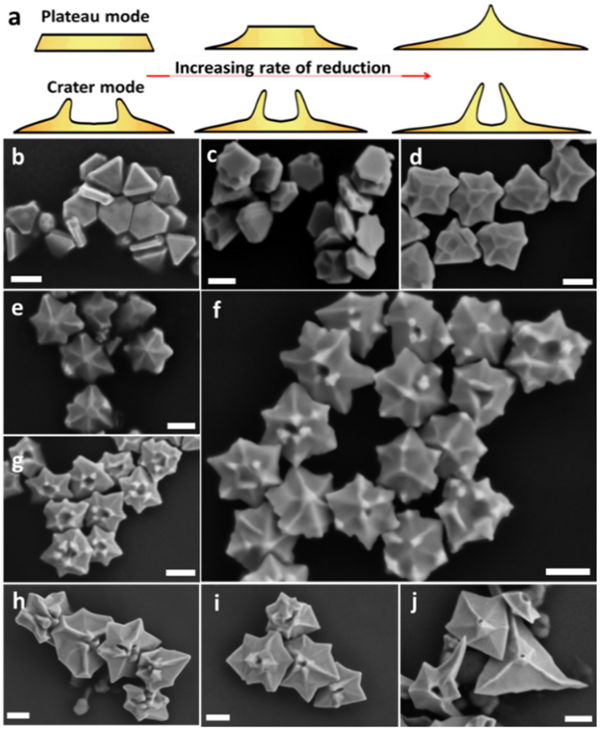

Fig. 4 Dependence of the nanohexagrams on the rate of reduction. (a) Schematics illustrating the evolution of the cross-section for plateau and crater mode. (b–g) The products obtained with the AA/$HAuCl_4$ ratio of 3, 6, 12, 24, 48, 96, respectively; and (h–j) the product nanohexagrams obtained with increasing amount of NaOH (0.25, 0.5, and 0.75 equivalent of AA), with the AA/$HAuCl_4$ ratio kept at 12. All scale bars are 200 nm.

pond to the early, middle, and late stages of growth. There are 3 trends to note during the growth: (1) the average edge length of the hexagons increases from 150 to 200, 250, 280, and 320 nm at the growth time of 20, 40, 90, 180 min, respectively; (2) the average size of the central crater decreases from 150, to 120, 100, and 80 nm with the growth time, respectively; (3) the ridges and spikes became taller with the growth, suggesting preferential growth at these ligand-deficient, high-curvature active sites. Obviously, these horizonal and vertical growths are correlated in giving the surface patterns.

Purely for the morphological comparison, our nanohexagrams have surface patterns in contrast to the I^--inhibited, flat Au nanostars reported by Wei *et al.*,[23] and have steeper ridges (Fig. 1c) than the faceted nanohexagrams by Xie *et al.*[24] In comparison to the hexagonal nanobowls from the wrapping growth mode,[25] the nanohexagrams of this work have more extruding corners at the horizontal direction, and steeper ridges and spikes at the vertical direction. While the reaction conditions are all different, essentially, our nanohexagrams have preferential growth at all tips, which could be explained by the ASG.

We varied the AA/$HAuCl_4$ ratio as the means to modulate the rate of Au reduction. As shown in Fig. 4b, Au was uniformly deposited on the nanoplate seeds at the lowest ratio (AA/$HAuCl_4$ = 3), which conforms with the conventional facet control. At a ratio of 6 (Fig. 4c, the plateau mode), defects appeared at the corners of the nanoplates, such that there are "bites" in the top plateau region making it smaller than the bottom plate. At a ratio of 12, the top plateau region became even smaller (100 ± 10 nm, Fig. 4d), only retained at the center of the nanohexagrams, and clear ridges could be identified at the periphery pointing at the corners. At the other extreme with a high AA/$HAuCl_4$ ratio of 96 (Fig. 4g, the crater mode), there is a concave crater at the center of each nanohexagram, which is surrounded by vertical spikes. Further increase of the AA/$HAuCl_4$ ratio to 144 and 192 did not give noticeable change of the product morphology.

In comparison to the plateau mode, it appears that the crater mode favors the high-curvature sites, including both the horizontal corners and vertical spikes. In between the two extremes of plateau and crater modes, nanohexagrams with central convex plateau and concave crater could coexist in a sample (Fig. 4f, AA/$HAuCl_4$ = 48), suggesting that they arise from two different pathways. Taking sample 4f as the reference point, lower AA/$HAuCl_4$ ratio leads to the plateau mode with increasing plateau area, whereas higher AA/$HAuCl_4$ ratio leads the crater mode with steeper ridges and spikes. The cross-section evolution corresponding to the plateau mode (Fig. 4b–e) and crater mode (Fig. 4g–j) is shown in Fig. 4a.

The main difference between the plateau and crater modes is the filling of the crater. That is, the edges are preferentially choked at the low deposition rates, whereas the center of nanoplate is preferentially choked at the high deposition rates. Typically, the ligand packing is known to depend on the facet and curvature,[19,26–28] but these two factors cannot explain the dependence of choking on the rate of reduction. Considering that the growth at any facet would always "refresh" the ligands on its surface, it is a natural consequence that the deposition rate would affect the rate of ligand refreshing, which in turn affects the degree of ligand packing. More specifically, the ligands near the edge are pinned by those at the high-curvature rims, making them more easily choked at the low deposition rates; whereas the crowded ligand patch at the center of the nanoplates are more difficult to replace simultaneously, making them more easily choked at the high deposition rates.

It is known that the rate of AA reduction increases with higher pH. Upon increase of the NaOH amount (0.25, 0.5, and 0.75 equivalent of AA, with AA/$HAuCl_4$ = 12), the resulting nanohexagrams have steeper ridges, relative to Fig. 4d. In Fig. 4j, the central plateau became abruptly extruding, in comparison to the smooth plateaus of Fig. 4d. The higher pHs appear to be effective in causing steeper extrusion as illustrated Fig. 1c.

Previously, we have shown 3 stages of the CTAB-induced ASG on decahedron seeds,[17] with additional curvature effects: (1) when the rate of Au deposition is low (not choked condition, or the normal facet control), the growth mode is the uniform expansion of all facets, similar to the observations in Fig. 4b. (2) At the intermediate rate of Au deposition (slightly choked condition), a few high-curvature corners are inhibited, whereas the rest of facets grow uniformly. This is consistent with the defective plateaus in Fig. 4c and d, except that the inhibition only applies to the vertical direction, not the horizontal direction. (3) With high rates of Au deposition (highly choked condition), the growth is focused onto a few sites, giving nanostructures with random spikes. This is consistent with the spiky nanohexagrams in Fig. 4f–g, except that there are multiple equivalent spikes at specific locations (as opposed to random sites). In terms of the shrinking plateau and steeper spikes, the overall trend is also consistent with faster Au deposition causing more focused growth at the active sites.

Fig. S7† demonstrates that even at low AA concentrations (AA/$HAuCl_4$ = 3), altering the reduction rate by pH results in a similar evolution of the morphology. Similarly, as shown in Fig. S8,† even though the homogeneity of the growth was reduced by the decreased CTAB concentration, the increased reduction rate also gave rise to more divergent growth. Hence, the mechanism is similar for the two systems, except that the growth on the nanoplates is highly site-selective, in terms of the orderly horizontal shape (hexagram) and rich variety of surface pattern.

Table 1 Structural features that could be explained by Active Surface Growth, not facet control

	Inequivalent growth	Facet control
Horizontal growth	Curved horizontal tips	Corners of regular angle
Vertical growth	Bulging features (ridge & crater)	Smooth (111) facet
Dihedral angle	“Curved facet” and ridges	Edges of regular angle

As summarized in Table 1, there are remarkable differences between the conventional facet control and the ASG, where the equivalent facets/sites would grow inequivalently. The rate of deposition is usually mild for the literature studies, and thus, the small deviations from facet control is often dismissed as minor interference from the chiral ligand or other factors such as curvature effects. By greatly increasing the rate of deposition, the structural features at the limiting conditions become irreconcilable with the arguments of facet control. In

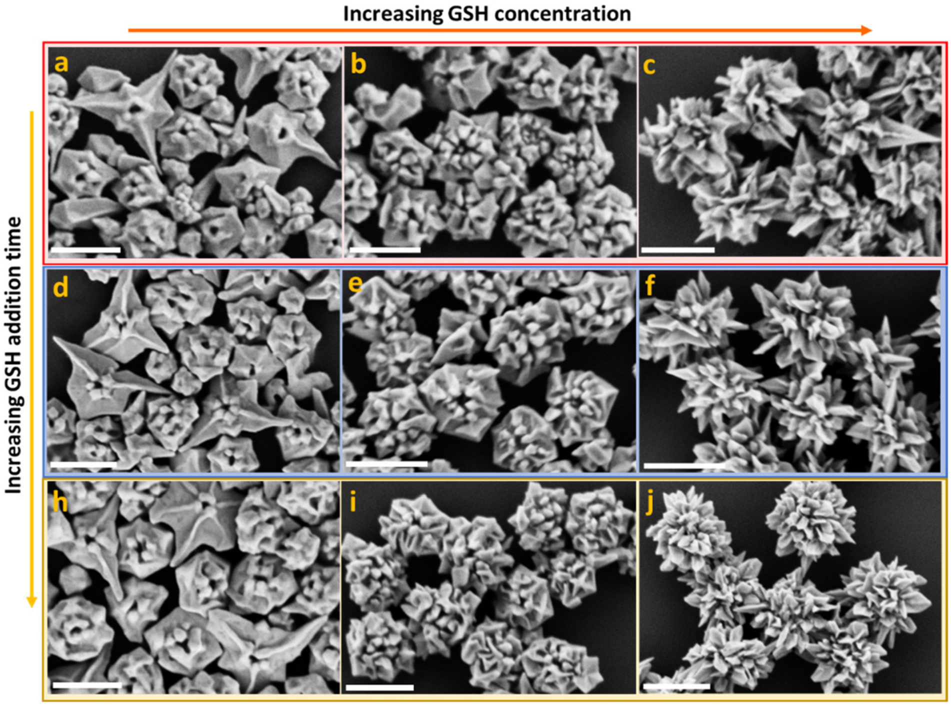

Fig. 5 Chiral induction half-way during the CTAB-controlled formation of Au nanohexagrams. The nanohexagrams were grown for 30, 60, and 100 min, before D-GSH of different concentrations was introduced. (a–c) 0.15, 0.72 and 3.6 μM GSH addition at 30 min, respectively. (d–f) 0.15, 0.72 and 3.6 μM GSH addition at 60 min, respectively. (h–j) 0.15, 0.72 and 3.6 μM GSH addition at 100 min, respectively. All scale bars are 500 nm.

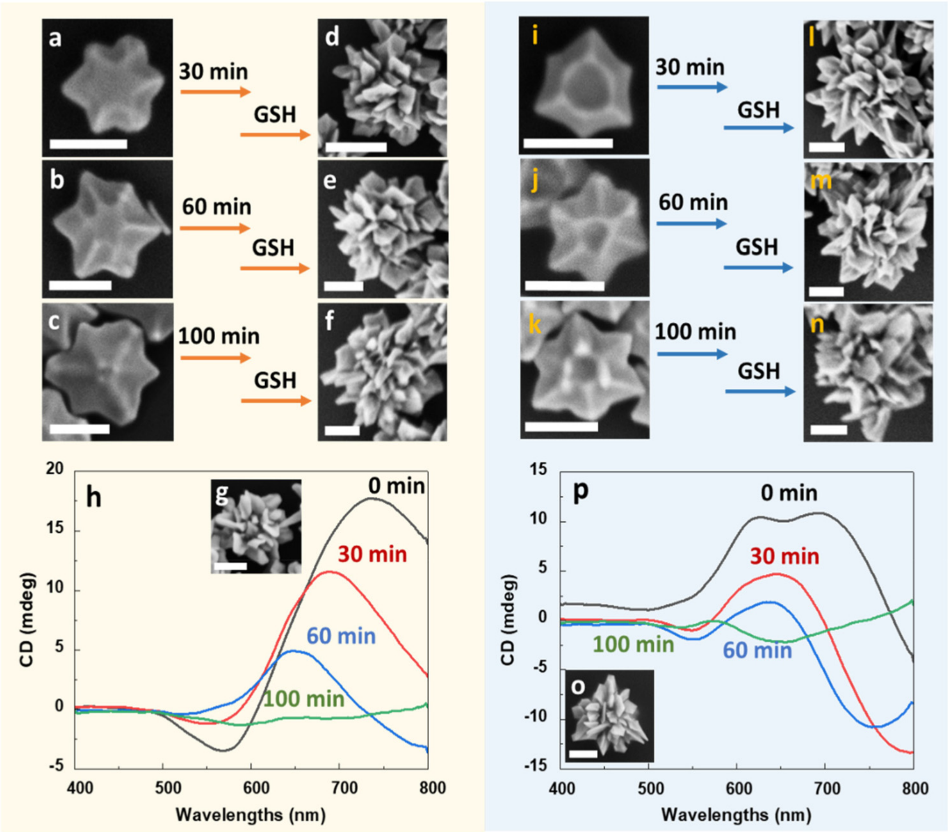

Fig. 6 Chiral induction half-way during the CTAB-controlled formation of Au nanohexagrams. The nanohexagrams were grown for 30, 60, and 100 min, before D-GSH (3.6 μM) was introduced: the experiments were carried out for both (a–h) the plateau mode (AA/$HAuCl_4$ = 12) and (i–o) the crater mode (AA/$HAuCl_4$ = 96), showing the nanohexagrams before (a–c, i–k) and after (d–f, l–n) after the chiral induction. The control samples are shown as insets (g and o), where D-GSH was added at the beginning of reaction. The CD spectra are shown in (h) and (p). All scale bars are 200 nm.

particular, the formation of orderly ridges under sole CTAB control poses interesting questions on the interplay between CTAB and chiral ligand.

Previously, Nam *et al.*[11] proposed that chiral pattern formation is from selective adsorption of chiral ligands on high index facets of seeds, with chirality emerging in later evolution stages. Building on this, a key finding in this work is that CTAB alone can generate highly curved surfaces. Thus, we investigated the timing of ligand addition on the chiral induction.

Increasing GSH concentration induced more complicate vertically extending nanostructures without clear chiral patterns (Fig. 5). The morphological evolution trend was similar for different GSH addition timings, however delayed introduction weakened the induced CD signal (Fig. S9†). This implies timing is crucial for inducing chirality. At lower GSH concentration, CD signals diminished, but the growth competition increased, with ~20% of particles developing irregular tips (Fig. 5a, d and h). Overall, these results suggest that both appropriately timed introduction and sufficient GSH levels are critical factors in coupling CTAB-mediated growth to yield chiral morphologies.

As shown in Fig. 6, we only modulated the time of GSH addition without changing other reaction parameters, to minimize the interference to the above model study. When the ligand GSH was included in the reaction before the addition of seeds (t = 0), the resulting CD signal was the strongest in the series, for both the plateau and crater modes (Fig. 6g and o). When GSH was added after the addition of seeds (t = 30, 60, 100 min), the resulting samples showed diminishing CD signals as shown in Fig. 6h and p, with a blue-shift of the peak position. The morphologies of the nanostructures do not show a clear trend, as the ridges and craters have turned into shattered vertical plates without recognizable pattern. We did not further modulate the reaction parameters because the morphological changes under combined control of CTAB and chiral ligands have been reported by our group and Zhang *et al.*[8,9]

A repeated set of experiments showed that the morphology of shattered vertical plates, the blue shift of the CD peaks, and the trend of decreasing intensity were reproducible. Hence, it appears that the chiral inducer needs to get involved early in the growth, otherwise its impact cannot be realized despite the obvious additional growth. It is likely that the stronger GSH ligand leads to more complete inhibition of the Au surface, and the more choked condition caused smaller depletion sphere[29] at the initial stage of heterogeneous nucleation. The resulting dense nucleation sites thus give the closely positioned vertical plates.

Experimental section

Instrumentation

SEM images were collected on a Gemini 450 Analytical Field Emission Scanning Electron Microscope operated under 5 kV. TEM images were collected by using Transmission Electron Microscopy operated at 200 kV (FEI-Talos F200X G2). The Circular Polarization data is obtained by the Rudolph Autopol IV-T circular dichroism spectrometer made by Applied Photophysics Ltd, America.

Chemicals

Hydrogen tetrachloroaurate(III) hydrate ($HAuCl_4 \cdot 3H_2O$, 99.9%), hexadecyltrimethyl-ammonium bromide (CTAB, ≥99%), L-ascorbic acid (AA, ≥99%), sodium borohydride ($NaBH_4$), sodium citrate ($C_6H_5O_7Na_3$), sodium hydroxide (NaOH), potassium iodide (KI) were purchased from Sigma-Aldrich. D-GSH (≥98%) was bought from GL Biochem., Ltd (Shanghai, China). Milli-Q water (resistivity 18.2 MΩ cm at 25 °C) was used in all experiments.

Synthesis of Au triangular nanoplates

The Au nanoplates were synthesized by a seed-mediated method.[30]

Synthesis of seed solution. $HAuCl_4$ (50 μL, 20 mM) and citrate (100 μL, 10 mM) were added to 4.75 mL of DI water. Then, $NaBH_4$ (100 μL, 0.1 M) was added to the mixture under vigorous stirring for 2 min. The color of the mixture immediately changed from yellow to brown. The seed solution was kept at room temperature for 2 h before use.

Synthesis of growth solution. $HAuCl_4$ (20 mM, 1.5 mL) was added to 108 mL of CTAB (0.025 M) solution with shaking. The colorless CTAB solution changed to yellow. Then, 600 μL of 0.1 M NaOH, 54 μL of KI (0.1 M), and 600 μL of 0.1 M AA were added to the above solution with gentle shaking. The color of the final solution was changed from yellow to colorless.

Synthesis of triangular Au nanoplates. First, 100 μL of seed solution was added to 900 μL of growth solution, and the mixture was shaken for 3 s. Second, 9 mL of growth solution was added to the above mixture, and the mixture was shaken for 4 s. Third, the obtained solution was mixed with 92 mL of growth solution *via* shaking for 6 s. After 30 min, the color of the mixture solution was changed from colorless to deep purple. It indicates the formation of Au nanoplates. After precipitation for 24 h, the nanoplates were accumulated in the bottom of the Erlenmeyer flask. After taking out the supernatant, the collected nanoplates were diluted with 10 mL of DI water. Finally, a green Au nanoplate solution was obtained.

Synthesis of Au nanohexagrams

CTAB (0.8 mL, 100 mM), $HAuCl_4$ (50 μL, 10 mM) and H_2O (3.95 mL) were placed into a 10 ml vial. Then 0.48 mL, 100 mM AA were added to the above solution quickly. After shaking the vial to mix the reactant, color of the mixture changed quickly from yellow to colorless. Then 50 μL triangular Au nanoplates were added to the above solution to initiate the growth. The growth was maintained at 30 °C for 3 h.

Modulation of growth rate

The experiments were prepared taking the same procedure with "Synthesizing Nano-hexagrams" Part. AA/$HAuCl_4$ ratio was tuned by changing the amount of AA: 15, 30, 60, 120 240 and 480 μL of AA for the ratio 3, 6, 12, 24, 48 and 96, respectively.

Secondary addition of chiral ligand

CTAB (0.8 mL, 100 mM), $HAuCl_4$ (50 μL, 10 mM) and H_2O (3.95 mL) were placed into a 10 ml vial. Then 0.48 mL, 100 mM AA (60 μL for plateau growth mode) were added to the above solution quickly. After shaking the vial to mix the reactant, color of the mixture changes quickly from yellow to colorless. For the addition of chiral ligand at 0 min, fresh prepared GSH solution (1.5 mg D-GSH powder dispersed in 10 mL water, 1.67, 8 and 40 μL was used for 0.15, 0.72 and 3.6 μM GSH concentration, respectively) and 50 μL triangular Au nanoplates were added to the above solution to initiate the growth. The growth was maintained at 30 °C for 3 h. For the addition at 30, 60 and 100 min, D-GSH was added after the initiation of the growth for certain reaction time.

Conclusion

Under the combined control of CTAB and chiral ligand, there are now several works reporting on the formation of chiral patterns.[6–9,11] Nam *et al.* have pioneered an explanation that the chiral patterns arise from the modulation of the stellated octahedron, *via* shifting and tilting of the R–S boundaries.[11] In contrast, we believe that the bulging features (ridges, spikes and chiral patterns) may arise from the ASG, where the differential deposition on the prochiral slopes caused consistent tilting of the ridges.[9] It is obvious that rich morphologies could be further derived from this synthetic system, and it would be more important to resolve the roles of CTAB *versus* chiral ligand, where further in-depth studies are imperative.

The fact that patterns of ridges and valleys could be synthesized under the sole control of CTAB provides a critical baseline for understanding the chiral synthesis. We prove beyond any doubt that the growth behaviors of this work under sole CTAB control belongs to the ASG. The curved horizontal tips, the strong correlation between each ridge and tip, and the steep ridges and craters (Fig. 1c) cannot be explained by the conventional facet control, but can be easily explained by the ASG.

Conflicts of interest

There are no conflicts to declare.

Acknowledgements

The authors gratefully acknowledge the financial support from the National Natural Science Foundation of China: General Program (No. 21673117, HC), Major Program (No. 91956109, HC) and Zhejiang Provincial Natural Science Foundation of China: Major Program (No. 2022XHSJJ002, HC), Hangzhou Municiple Funding, Team of Innovation (No. TD2022004) and Foundation of Westlake University. The authors thank Westlake Center for Micro/Nano Fabrication for the facility support and technical assistance.

References

1 Y. Wang, J. Xu, Y. Wang and H. Chen, *Chem. Soc. Rev.*, 2013, **42**, 2930.
2 A. Mondal, R. Toyoda, R. Costil and B. L. Feringa, *Angew. Chem.*, 2022, **134**, e202206631.
3 V. M. Kadiri, C. Bussi, A. W. Holle, K. Son, H. Kwon, G. Schütz, M. G. Gutierrez and P. Fischer, *Adv. Mater.*, 2020, **32**, 2001114.
4 Z. Wu, J. Troll, H.-H. Jeong, Q. Wei, M. Stang, F. Ziemssen, Z. Wang, M. Dong, S. Schnichels, T. Qiu and P. Fischer, *Sci. Adv.*, 2018, **4**, eaat4388.
5 J. C. Love, L. A. Estroff, J. K. Kriebel, R. G. Nuzzo and G. M. Whitesides, *Chem. Rev.*, 2005, **105**, 1103.
6 L. Xu, X. Wang, W. Wang, M. Sun, W. J. Choi, J.-Y. Kim, C. Hao, S. Li, A. Qu, M. Lu, X. Wu, F. M. Colombari, W. R. Gomes, A. L. Blanco, A. F. De Moura, X. Guo, H. Kuang, N. A. Kotov and C. Xu, *Nature*, 2022, **601**, 366.
7 S. W. Im, E. Jo, R. M. Kim, J. H. Han and K. T. Nam, *Adv. Opt. Mater.*, 2023, 2300037.
8 Y. Tao, L. Sun, C. Liu, G. Yang, X. Sun and Q. Zhang, *Small*, 2023, **19**, 2301218.
9 Y. Zheng, Q. Wang, Y. Sun, J. Huang, J. Ji, Z.-J. Wang, Y. Wang and H. Chen, *Adv. Opt. Mater.*, 2023, 2202858.
10 J. Yan, Y. Chen, S. Hou, J. Chen, D. Meng, H. Zhang, H. Fan, Y. Ji and X. Wu, *Nanoscale*, 2017, **9**, 11093.
11 H.-E. Lee, H.-Y. Ahn, J. Mun, Y. Y. Lee, M. Kim, N. H. Cho, K. Chang, W. S. Kim, J. Rho and K. T. Nam, *Nature*, 2018, **556**, 360.
12 J. Kim, I. Jung, M. J. Oh, H. Hilal, W. Park and S. Park, *Chem. Mater.*, 2023, **35**(10), 3976.
13 Y. Ma, Q. Kuang, Z. Jiang, Z. Xie, R. Huang and L. Zheng, *Angew. Chem., Int. Ed.*, 2008, **47**, 8901.
14 J. Mosquera, D. Wang, S. Bals and L. M. Liz-Marzán, *Acc. Chem. Res.*, 2023, **56**, 1204.
15 B. Nikoobakht and M. A. El-Sayed, *Langmuir*, 2001, **17**, 6368.
16 S. Gómez-Graña, F. Hubert, F. Testard, A. Guerrero-Martínez, I. Grillo, L. M. Liz-Marzán and O. Spalla, *Langmuir*, 2012, **28**, 1453.
17 Y. Zheng, J. Zong, T. Xiang, Q. Ren, D. Su, Y. Feng, Y. Wang and H. Chen, *Sci. China: Chem.*, 2022, **65**, 1299.
18 R. Xiao, J. Jia, R. Wang, Y. Feng and H. Chen, *Acc. Chem. Res.*, 2023, **56**(12), 1539.
19 Y. Li, H. Lin, W. Zhou, L. Sun, D. Samanta and C. A. Mirkin, *Sci. Adv.*, 2021, **7**, eabf1410.
20 S. Yang, H. Li, R. Liu, C. Wang, J. Yu, S. Li, Y. Wang and H. Chen, *Inorg. Chem. Front.*, 2022, **9**, 4136.
21 J. E. Millstone, W. Wei, M. R. Jones, H. Yoo and C. A. Mirkin, *Nano Lett.*, 2008, **8**, 2526.
22 O. M. Magnussen, *Chem. Rev.*, 2002, **102**, 679.
23 W. Guo, A. C. Johnston-Peck, Y. Zhang, Y. Hu, J. Huang and W. D. Wei, *J. Am. Chem. Soc.*, 2020, **142**, 10921.
24 Q. Jiang, Z. Jiang, L. Zhang, H. Lin, N. Yang, H. Li, D. Liu, Z. Xie and Z. Tian, *Nano Res.*, 2011, **4**, 612.
25 S. Yang, Y. Zheng, G. He, M. Zhang, H. Li, Y. Wang and H. Chen, *Chem. Commun.*, 2022, **58**, 6128.
26 B. E. Janicek, J. G. Hinman, J. J. Hinman, S. H. Bae, M. Wu, J. Turner, H.-H. Chang, E. Park, R. Lawless, K. S. Suslick, C. J. Murphy and P. Y. Huang, *Nano Lett.*, 2019, **19**, 6308.
27 T. Jiang, J. Zong, Y. Feng and H. Chen, *Precis. Chem.*, 2023, **1**, 94.
28 F. Wang, S. Cheng, Z. Bao and J. Wang, *Angew. Chem., Int. Ed.*, 2013, **52**, 10344.
29 Y. Feng, Y. Wang, X. Song, S. Xing and H. Chen, *Chem. Sci.*, 2017, **8**, 430.
30 Y. Huang, A. R. Ferhan, Y. Gao, A. Dandapat and D. H. Kim, *Nanoscale*, 2014, **6**, 6496.